

RESEARCH ARTICLE

Is Doping of Spiro-OMeTAD a Requirement for Efficient and Stable Perovskite Indoor Photovoltaics?

Sami Toikkonen¹, G. Krishnamurthy Grandhi¹, Shaoyang Wang², Bora Baydin³, Basheer Al-Anesi¹, L. Krishnan Jagadamma², and Paola Vivo^{1*}

¹Hybrid Solar Cells, Faculty of Engineering and Natural Sciences, Tampere University, P.O. Box 541, Tampere FI-33014, Finland. ²Energy Harvesting Research Group, SUPA, School of Physics and Astronomy, University of St Andrews, North Haugh, St Andrews KY16 9SS, UK. ³Department of Chemistry, Yildiz Technical University, 34220 Esenler, Istanbul, Turkey.

*Address correspondence to: paola.vivo@tuni.fi

Lead halide perovskite (LHP) photovoltaics deliver high voltages even under low-light illumination intensities, thus emerging as a promising indoor photovoltaic (IPV) technology. The doping of the 2,2',7,7'-tetrakis(*N,N*-di-*p*-methoxyphenylamino)-9,9'-spirobifluorene (Spiro-OMeTAD) hole-transport layer (HTL) is the most widely adopted strategy for high-performance LHP-based solar cells. Yet, the importance of Spiro-OMeTAD doping is unclear in the context of indoor photovoltaics. In this report, we examine the role of the traditional Spiro-OMeTAD dopants on the performance of LHP-based IPVs. The diminished influence of the series resistance under indoor lighting leads to an improved fill factor of IPV devices even in the absence of the dopants. The pristine (dopant-free) Spiro-OMeTAD HTL ensures a power conversion efficiency (PCE) as high as 25.6% at 1,000 lux, comparable to that of 29.7% in the presence of the dopants, and an open-circuit voltage of ≈ 0.65 V even at 50 lux. The undoped Spiro-OMeTAD-containing devices exhibit a $\approx 25\%$ gain in their PCE under long-term and continuous white light illumination at the maximum power point, thus leading to the PCE values on par or higher than those of employing doped Spiro-OMeTAD. Furthermore, the current–voltage hysteresis behavior of the undoped Spiro-OMeTAD-containing devices remains unchanged in the 100 to 1,000 lux light-intensity range, unlike the case of doped Spiro-OMeTAD HTL. Our findings suggest that the dopants in Spiro-OMeTAD HTL are not required to achieve efficient, stable, and reliable IPV performance, and the optimization of the various device constituents for outdoor solar cell applications may not necessarily lead to the best performance for indoor photovoltaics.

Introduction

Lead halide perovskites (LHPs) are attractive semiconductors for the next-generation solar cells, achieving record-breaking power conversion efficiency (PCE) values above 26% [1]. The exceptional performance of LHP photovoltaics is mainly attributed to the high defect tolerance and self-healing of LHP absorbers [2] and the optimal design and engineering of the other device constituents, especially the charge-transport layers. Among the many hole-transport materials that have been screened over the years, 2,2',7,7'-tetrakis(*N,N*-di-*p*-methoxyphenylamino)-9,9'-spirobifluorene (Spiro-OMeTAD) still remains the preferred choice for efficient LHP-based solar cells [3,4]. It is, however, well-established that, to ensure high hole mobility and electrical conductivity of Spiro-OMeTAD and favorable energy band alignment with the perovskite layer, it is necessary to dope the Spiro-OMeTAD hole-transport layer (HTL) with molecular additives, typically 4-*tert*-butylpyridine (*t*BP), bis(trifluoromethane) sulfonimide lithium salt (Li-TFSI), and tris[2-(1*H*-pyrazol-1-yl)-4-*tert*-butylpyridine]cobalt(III)tri[bis(trifluoromethane)

sulfonimide] (FK209 Co(III)). A doped Spiro-OMeTAD HTL is essential to suppress the voltage losses in LHP-based solar cells and enable high PCE, which would otherwise be limited to $<10\%$ for devices with a pristine (undoped) Spiro-OMeTAD layer [5–7]. Nevertheless, under operational conditions (solar illumination, bias, and heat), dopants are known to cause device degradation by deteriorating the perovskite and other device layers through pinhole formation facilitated by Li^+ migration or evaporation of *t*BP [7–10]. Therefore, it is widely acknowledged that the use of dopant-free HTLs, which would not detrimentally affect the device efficiency, is the optimal choice for operationally stable LHP solar cells [10].

In addition to the sunlight, LHPs have proved to also harvest the artificial indoor light very efficiently, with a record indoor power conversion efficiency (PCE(*i*)) in indoor photovoltaics (IPVs) of $\approx 41\%$ [11,12]. There is a growing interest on IPVs, motivated by the need of finding a sustainable solution to power the rapidly growing number of battery-free, low-cost, and wireless sensors requiring micro- to milliwatt power within the Internet of Things (IoT) ecosystem [13]. Most LHP-based IPVs

Citation: Toikkonen S, Grandhi GK, Wang S, Baydin B, Al-Anesi B, Jagadamma LK, Vivo P. Is Doping of Spiro-OMeTAD a Requirement for Efficient and Stable Perovskite Indoor Photovoltaics? *Adv. Devices Instrum.* 2024;5:Article 0048. <https://doi.org/10.34133/adi.0048>

Submitted 30 December 2023

Accepted 3 March 2024

Published 5 June 2024

Copyright © 2024 Sami Toikkonen et al. Exclusive licensee Beijing Institute of Aerospace Control Devices. No claim to original U.S. Government Works. Distributed under a Creative Commons Attribution License 4.0 (CC BY 4.0).

Downloaded from <https://spj.science.org> at Tampere University on June 24, 2024

reported to date also use doped Spiro-OMeTAD as the HTL [11,14,15]. This choice is primarily due to the ability of the dopants to suppress the resistive losses, thereby improving the PCE of solar cells. This is the case even though the intensity of indoor lighting is 2 orders of magnitude lower than that of the simulated sunlight (air mass [AM] 1.5G, 100 mW cm⁻²), commonly referred to as 1-Sun illumination. However, no study has so far revealed the impact of the dopants on the figures of merits of LHP-based IPV. Indeed, the performance under 1-Sun illumination does not necessarily translate to low-intensity lighting, as proved for other photovoltaic technologies like copper indium gallium selenide and silicon [16].

The IPV field is still in its early stages, with the primary focus being on enhancing PCE(i) and the operational stability aspects often overlooked. However, understanding the real-world stability patterns of IPV, backed by comprehensive stability datasets, is crucial for assessing the market potential of LHP-based IPV, especially considering the multi-year life expectancy of IPV-powered IoT sensors. Therefore, it is important to investigate the operational stability of IPV devices containing doped Spiro-OMeTAD. This will help determine if doping Spiro-OMeTAD is indeed the best strategy for LHP-based IPV devices, in terms of both performance and stability.

In this study, we examine how dopants in the Spiro-OMeTAD HTL affect the efficiency and stability of LHP-based photovoltaic devices under conditions of simulated sunlight (1-Sun) or artificial white light-emitting diode (WLED) indoor lighting. Despite the modest expected PCE of the devices using undoped Spiro-OMeTAD compared to their doped Spiro-OMeTAD counterparts, the former show substantially improved performance at low-light intensities, with their PCE(i) nearing that of the cells using doped Spiro-OMeTAD. We delve into the factors contributing to this notable efficiency increase in IPV devices using the undoped HTL. Beyond the typical 1,000 lux indoor illumination, we also explore the influence of doped and undoped Spiro-OMeTAD HTLs on the performance and current density (J)-voltage (V) hysteresis of LHP devices under extremely low-light WLED intensities, going as low as 50 lux. Lastly, we discuss the indoor operational stability of LHP devices, comparing those with and without dopants in the Spiro-OMeTAD layer.

Materials and Methods

Materials

Formamidinium iodide (FAI), methyl ammonium bromide (MABr), and 30 NRD titanium dioxide (TiO₂) paste were purchased from Greatcell Solar Materials. Lead bromide (PbBr₂, >98%) and lead iodide (PbI₂, >98%) were acquired from TCI. Cesium iodide (CsI) was purchased from abcr. Titanium diisopropoxide bis(acetylacetonate) stock solution (75 wt. % in 2-propanol), dimethyl sulfoxide (DMSO, anhydrous, ≥99.9%), dimethyl formamide (DMF, anhydrous, 99.8%), chlorobenzene (anhydrous, 99.8%), acetonitrile (99.9%), *t*BP (98%), and Li-TFSI (99.95%) were purchased from Sigma-Aldrich. Spiro-OMeTAD (>99.5%) was purchased from Lumtec. FK209 Co(III) (>95%) was acquired from Dyenamo. All reagents and solvents were used as received without additional purification.

Fabrication of perovskite photovoltaic cells

The photovoltaic cells were fabricated onto pre-etched fluorine-doped tin oxide (FTO)-coated glass substrates (OPV Tech) with dimensions of 2.54 cm × 2.54 cm × 0.22 cm. The substrates

were cleaned by first brushing with 2 v/v % Mucosal solution in deionized water and then kept in a sonication bath in deionized water, acetone, and 2-propanol for 15 min each following drying with N₂ flow. The substrates were UV-ozone-treated for 10 min prior to the next step.

A compact TiO₂ (c-TiO₂) layer was deposited on the substrates via spray pyrolysis at 450 °C followed by 45 min sintering at 450 °C in air. The precursor solution was prepared from a titanium diisopropoxide bis(acetylacetonate) stock solution by diluting it with 2-propanol with typical amounts of 1.15 ml of the stock solution per 5 ml of 2-propanol. A mesoporous TiO₂ (m-TiO₂) layer was prepared by spin coating 80 μl of 30 NRD TiO₂ nanoparticle paste suspension in ethanol (150 mg ml⁻¹) at 4,000 rpm for 10 s (including 2,000 rpm s⁻¹ acceleration), followed by annealing at 100 °C for few minutes, and then calcinated at 450 °C for 30 min with 45 min ramp time in heating. The substrates were then cooled down to 200 °C and transferred to a N₂ filled glove box for the further steps.

The CsMAFA-Pb triple-cation perovskite (Cs_{0.05}(MA_{0.17}FA_{0.83})_{0.95}Pb(I_{0.83}Br_{0.17})₃) was prepared according to Saliba et al. [17]. The perovskite precursor solution was prepared the day prior to the film deposition by mixing FAI (0.95 M), MABr (0.19 M), PbBr₂ (0.20 M), and PbI₂ (1.1 M) in a mixed solvent of DMSO:DMF (1:4 volume ratio). CsI was pre-dissolved in DMSO (1.5 M) and 40 μl of the CsI solution was added into 1 ml of the perovskite precursor solution, which was left under stirring until it is used (≈24 h). Sixty microliters of the perovskite precursor solution was spin coated on top of FTO|c-TiO₂|m-TiO₂ substrate first at 1,000 rpm for 10 s and then accelerated to 6,000 rpm for 20 s. Chlorobenzene (100 μl) was dropped onto the substrate 5 s before the spin coating finished (antisolvent treatment). The perovskite films were annealed at 110 °C for 60 min. After annealing, the substrates were cooled down for a few minutes prior to deposition of Spiro-OMeTAD HTL. Spiro-OMeTAD solution was prepared by dissolving Spiro-OMeTAD in chlorobenzene to have 36.2 mg ml⁻¹ concentration. For the doped Spiro-OMeTAD solution, *t*BP, Li-TFSI (520 mg ml⁻¹ in acetonitrile), and FK209 Co(III) (300 mg ml⁻¹ in acetonitrile) were added in volumes of 14.4 μl, 8.8 μl, and 14.5 μl, respectively, into 1 ml of Spiro-OMeTAD solution. Spiro-OMeTAD solution (80 μl; doped or undoped) was dynamically spin coated onto the perovskite films at 1,800 rpm for 30 s. Samples were then kept in a dry cabinet (≈15% to 20% relative humidity [RH]) overnight before top electrode deposition. A gold (Au) layer (80 to 100 nm thick) was thermally evaporated onto the samples with a OPTIvap Vacuum Deposition Tool (MBraun) to finalize the photovoltaic cells with an active area of 12 mm².

Device characterization

The Litos Lite system (FLUXiM AG, Switzerland) was used to record the J - V reverse and forward sweeps (scan rate 50 mV s⁻¹) and maximum power point (MPP) tracking from the prepared photovoltaic cells under simulated sunlight. The AM 1.5G simulated sunlight (1-Sun, 100 mW cm⁻²) was obtained with an A++A+A solar simulator (Sinus-70 LED simulator from Wavelabs). J - V curves and stable power output (SPO) were measured in air, while longer MPP tracking was done under N₂ atmosphere. 7-mm² aperture masks were used. MPP tracking was performed under continuous 1-Sun illumination.

A Philips HUE WLED bulb with adjustable color temperature was used as the lightning source for the indoor photovoltaic

characterization set at 4,000 K color temperature. Illuminance level of the lamp was monitored with a calibrated lux meter (Digi-Sense). The power density of the WLED bulb at different illuminances was determined using a Konica Minolta CL-500A Illuminance Spectrophotometer at varying illuminances. For example, at 1,000 lux WLED intensity, a power density of $\approx 0.32 \text{ mW cm}^{-2}$ was measured on the photovoltaic cell surface. J - V reverse and forward sweeps (scan rate 50 mV s^{-1}) and SPO were recorded with a Keithley 4250 source-monitor unit using a 4-wire setup. Measurements were performed inside a black box and 7-mm^2 aperture masks were used. MPP tracking under indoor lightning was performed using the Litos Lite system under N_2 atmosphere either under continuous illumination or in 8 h light–16 h dark cycles. An intensity of 5,000 lux ($\approx 1.60 \text{ mW cm}^{-2}$) was used to acquire indoor MPP tracking data with an adequate signal-to-noise ratio, and aperture masks were not used in this case.

External quantum efficiency (EQE) spectra were measured in the range of 350 to 850 nm using a quantum efficiency measurement device (QuantX-300, Newport). Transient photovoltage and transient photocurrent measurement were carried out with a characterization platform, Paios (FLUXiM AG, Switzerland).

Results and Discussion

We adopted the conventional superstrate configuration of glass|FTO|c-TiO₂|m-TiO₂+CsMAFA-Pb|Spiro-OMeTAD|Au

to fabricate mesoporous triple-cation LHP photovoltaic cells, as shown in Fig. 1A. The Spiro-OMeTAD HTL was deposited with (the corresponding devices being referred to as “Doped Spiro”) and without (the corresponding devices being referred to as “Undoped Spiro”) the widely used dopants, namely, Li-TFSI, *t*BP, and FK209 Co(III). All the device fabrication details can be found in Materials and Methods. The normalized EQE spectra of the Doped Spiro and Undoped Spiro devices are plotted along with 1-Sun spectrum (AM 1.5G) and the emission spectrum of a WLED (4,000 K color temperature) in Fig. 1B. It is evident from the figure that the EQE spectral distribution of the devices covers the complete spectral range of the WLED with a theoretical maximum PCE of 50% to 55% (for a bandgap of $\approx 1.6 \text{ eV}$) [18] under a 1,000-lux intensity of $\approx 0.3 \text{ mW cm}^{-2}$, whereas the theoretically predicted highest PCE that can be achieved under standard 1-Sun illumination (100 mW cm^{-2}) is $\approx 30\%$ [19]. We first characterized both the Doped Spiro and Undoped Spiro devices under standard 1-Sun illumination by recording J - V curves in both forward and reverse bias sweeping directions. The statistical distributions of PCE values of the 2 types of devices are shown in Fig. 1C. As expected, the Doped Spiro devices demonstrated superior performance than the Undoped Spiro ones, with the respective average PCE values of 17.7% and 6.2%. The major performance loss factor in the latter case is their poor fill factors (FFs) of $\approx 30\%$ vs. FFs of 70% to 75% in the case of Doped Spiro cells (see Fig. 1D and Table 1). The low FF of the Undoped Spiro devices, originating from the typical S-shaped J - V curve, can be mainly attributed to

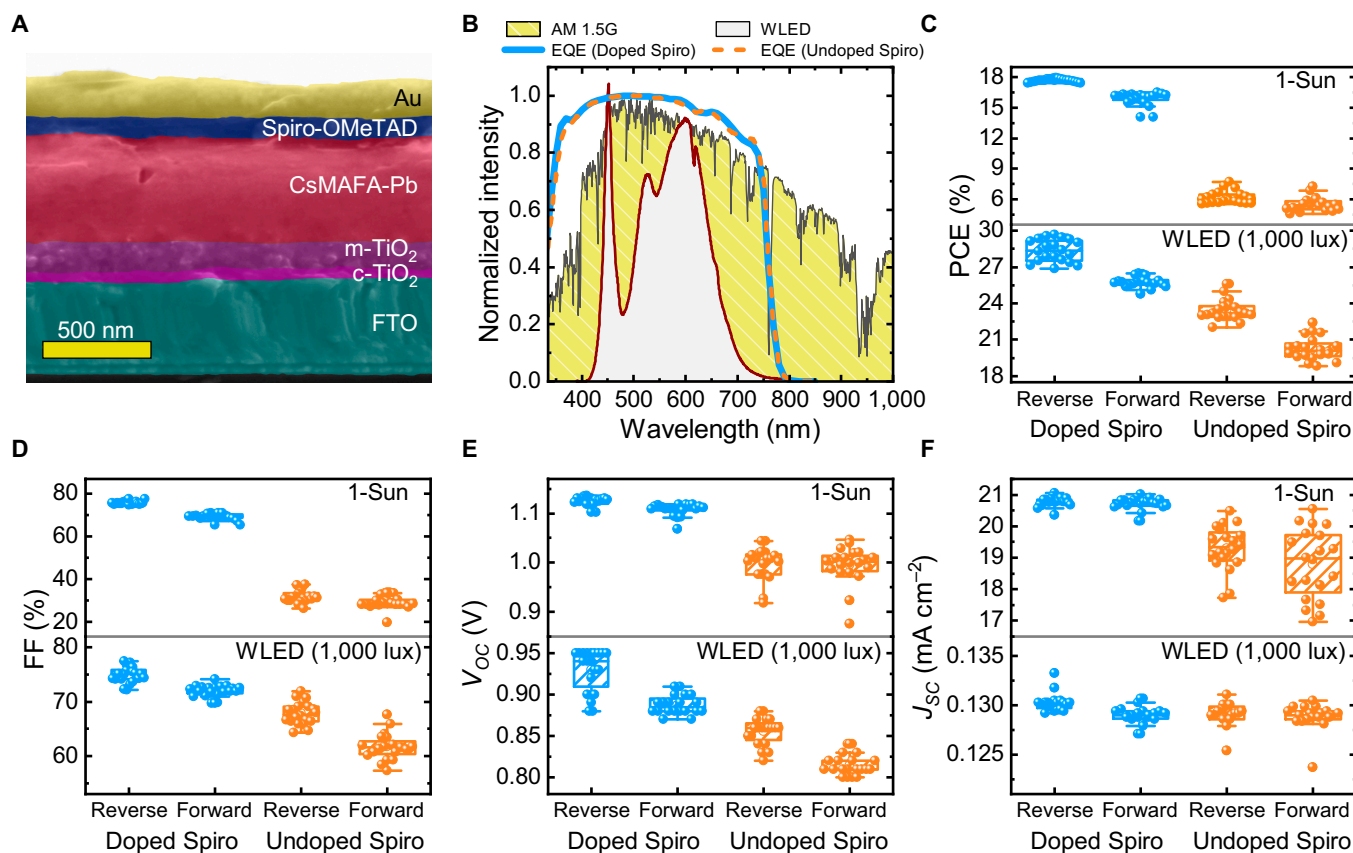


Fig. 1. Photovoltaic performance of Doped Spiro and Undoped Spiro devices under 1-Sun and 1,000 lux WLED illumination. (A) A representative SEM cross-sectional image of the devices. (B) Normalized 1-Sun and WLED spectra along with the EQE spectra of the devices. Statistical distributions (20 devices) of (C) PCE, (D) FF, (E) V_{oc} , and (F) J_{sc} of the devices under 2 illuminations derived from the J - V scans in reverse and forward directions.

Table 1. Average photovoltaic parameters (20 devices in each case) under 1-Sun and 1,000 lux WLED illuminations. Champion cell photovoltaic parameters are given in the brackets. H-index = $(PCE_{REV}/PCE_{FOR}) \times 100\% - 100\%$.

Device	Illumination source	J–V scan direction	PCE (%)	FF (%)	J_{SC} (mA cm ⁻²)	V_{OC} (V)	H-index (%)
Doped Spiro	1-Sun	Reverse	17.7 ± 0.2 (18.0)	75.7 ± 0.7 (75.4)	20.8 ± 0.1 (21.1)	1.12 ± 0.01 (1.13)	10.0 ± 2.9 (9.4)
		Forward	15.9 ± 0.5 (16.3)	69.4 ± 1.3 (69.2)	20.7 ± 0.2 (21.0)	1.11 ± 0.01 (1.12)	
	1,000 lux WLED	Reverse	28.3 ± 0.9 (29.7)	74.9 ± 1.5 (77.2)	0.130 ± 0.001 (0.129)	0.93 ± 0.03 (0.95)	10.0 ± 3.0 (12.2)
		Forward	25.8 ± 0.4 (26.4)	72.0 ± 1.1 (72.6)	0.129 ± 0.001 (0.128)	0.89 ± 0.01 (0.91)	
Undoped Spiro	1-Sun	Reverse	6.2 ± 0.6 (7.7)	31.9 ± 2.8 (36.0)	19.3 ± 0.7 (20.5)	1.00 ± 0.03 (1.04)	11.0 ± 4.9 (5.8)
		Forward	5.5 ± 0.7 (7.2)	29.3 ± 2.3 (33.7)	18.8 ± 1.1 (20.5)	0.99 ± 0.04 (1.05)	
	1,000 lux WLED	Reverse	23.4 ± 0.8 (25.6)	67.8 ± 2.1 (71.9)	0.129 ± 0.001 (0.129)	0.86 ± 0.02 (0.88)	15.7 ± 3.1 (14.3)
		Forward	20.3 ± 1.0 (22.4)	61.7 ± 2.4 (67.6)	0.129 ± 0.001 (0.129)	0.82 ± 0.01 (0.82)	

the poor hole extraction and transport ability of pristine Spiro-OMeTAD arising from the intrinsically low hole mobility (in the order of 10^{-4} to 10^{-5} cm² V⁻¹ s⁻¹) and the consequent high series resistance (R_s) of the devices [6,20]. Indeed, the Undoped Spiro-OMeTAD devices exhibit an order of magnitude higher R_s of $\approx 100 \pm 3$ Ω cm² compared to the doped counterpart ($R_s = 4 \pm 1$ Ω cm²) (see Table S1). Furthermore, the average open-circuit voltage (V_{OC}) and short-circuit current density (J_{SC}) values of the Doped Spiro devices are relatively higher than those of the undoped Spiro devices (Fig. 1E and F), which is attributed to the dopant-induced difference in the energetics between the 2 devices [7,21,22].

The discrepancy in the photovoltaic parameters obtained from the reverse and forward J – V scans suggests the presence of hysteresis (Fig. S1A), as widely reported for perovskite-based devices [23,24]. The champion Doped Spiro device exhibits PCE values of 18.0% and 16.3% under reverse and forward scans, respectively. The corresponding stabilized PCE is 17.8% under a voltage bias of 0.93 V (Fig. S1B), as obtained by conducting the SPO near the MPP. The stabilized PCE value lies between the PCE values from reverse and forward J – V scans. The hysteresis is also present in the Undoped Spiro samples and the champion device demonstrated a stabilized PCE of 7.7% (Fig. S1B). The average J – V hysteresis index (H-index) of Doped and Undoped Spiro devices is around 10% (Table 1). The H-index, while useful, is not a steady-state metric as it overlooks extrinsic scanning factors like scan speed, range, direction, measurement delay, light soaking, and pre-biasing. Despite its various interpretations, it is still valuable for comparing hysteresis between Undoped Spiro and Doped Spiro devices whose J – V curves were obtained under identical scan parameters. However, we advise readers to be cautious when using H-index values for hysteresis quantification across different studies.

Furthermore, both types of devices possess a peak EQE value of $\approx 90\%$ in the 450- to 600-nm wavelength range (Fig. S1C), where a major portion of the emission intensity of the WLED lies (Fig. 1B). Consequently, the devices are anticipated to perform efficiently under low-intensity WLED light. We investigated the IPV performance of the 2 types of the devices under variable ambient illuminance levels, from 1,000 lux (Fig. 2A and B) down to 50 lux (Fig. 2C and D). The J – V curves at 1,000 lux for the champion devices of the 2 types are displayed in Fig. 2A. The average PCE of the Doped Spiro devices increases from 17.7% under 1-Sun (100 mW cm⁻²) to 28.3% under 1,000 lux WLED illumination (0.32 mW cm⁻²) with an indoor PCE (PCE(i)) of 29.7% (27.3% stabilized PCE(i)) and a corresponding power output of 87.4 μW cm⁻² for the champion device. The PCE(i) is comparable to the value recently reported for a planar device architecture employing a similar triple-cation perovskite absorber and a tin oxide electron transporting layer [25].

The highest PCE(i) at 1,000 lux for Undoped Spiro devices (25.6%, with 23.4% being the stabilized PCE(i)) is 3 times higher than the PCE (7.7%) of the same devices under 1-Sun illumination. The power output of the Undoped Spiro samples is 74.9 μW cm⁻² at 1,000 lux. Such a remarkable performance jump is driven by a 2-fold FF enhancement under indoor vs. 1-Sun illumination, unlike the nearly unchanged FF values in the case of the Doped Spiro devices (Table 1). We further observed a continuous increase in the FF of the Undoped Spiro devices when lowering the light intensity from 1-Sun to 0.1-Sun (Fig. 3A). The FF enhancement indicates reduced influence of the high series resistance of the devices at low-light intensities [26]. In addition, the shunt resistance (R_{SH}) of the Undoped Spiro devices under 1,000 lux WLED and 1-Sun illuminations, extracted from the corresponding J – V curves, is 2 to 3 orders of magnitude higher under artificial indoor light ($2.5 \pm 0.2 \times 10^5$ Ω cm²)

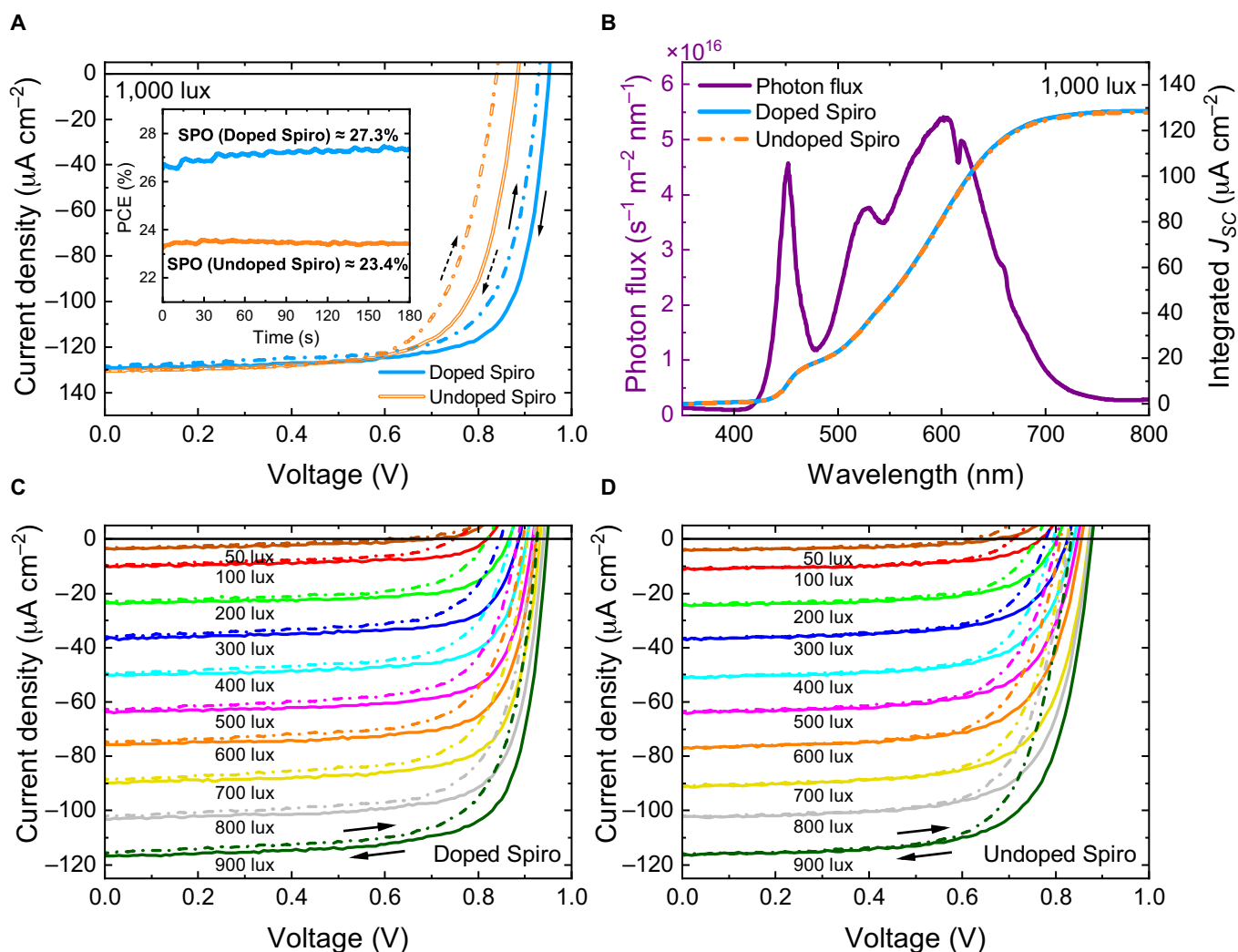


Fig. 2. IPV performance of Doped and Undoped Spiro devices. (A) J - V curves and SPOs at bias voltages of 0.79 V for Doped Spiro and 0.70 V for Undoped Spiro devices at 1,000 lux. (B) Photon flux density spectrum of the WLED at 1,000 lux and the integrated J_{sc} profiles. J - V curves in the 50 to 900 lux range for (C) Doped Spiro and (D) Undoped Spiro devices.

than under 1-Sun illumination ($0.6 \pm 0.1 \times 10^3 \Omega \text{ cm}^2$). While a high shunt resistance is necessary for photovoltaic devices operating under low-light intensity conditions, the influence of the series resistance diminishes (conversely to the case of high-light intensities) [26]. This further explains the major improvement in FF and, thus, performance of the Undoped Spiro device under dim light illumination. Furthermore, the photocurrent values extracted from the J - V sweeps (J_{sc}^{J-V}) are nearly the same (i.e., 129 to 130 $\mu\text{A cm}^{-2}$) for the 2 devices and lower than the theoretical limit of 140 cm^{-2} at a fixed incidence power density of 0.3 mW cm^{-2} [27].

The current density value (J_{sc}^{EQE}), calculated using a combination of their EQE spectra and the incident photon flux density spectrum, is $\approx 128 \mu\text{A cm}^{-2}$ (Fig. 2B). This leads to a small mismatch of $\leq 1\%$ between J_{sc}^{EQE} and J_{sc}^{J-V} , in turn verifying the excellent reliability in our IPV measurements.

Next, we investigated the IPV performance of the 2 champion devices under intensities lower than 1,000 lux (i.e., 50 to 900 lux), with the corresponding incident power densities in the 0.016 to 0.288 mW cm^{-2} range. The indoor light-intensity dependent J - V curves of Doped Spiro and Undoped Spiro

devices are presented in Fig. 2C and D, respectively. It is evident from Fig. 2C and Table 2 that the H-index of the Doped Spiro device gradually increases with the lowering of the WLED intensity—from 8% at 1,000 lux to 19% at 200 lux and even to 33% at 100 lux, which suggests its unreliable IPV performance under very low-light intensities. Interestingly, the H-index of the Undoped Spiro device remains instead in the 5% to 8% range under the same illumination intensities (Table 2). As light intensity diminishes, the increased hysteresis of the Doped Spiro device contrasts with the typically observed phenomenon where the activation energy barrier for ion migration is suppressed at high-light intensities [28,29]. This suggests that ion migration is not the main contributing factor for the observed J - V hysteresis under low-intensity artificial indoor lighting for the Doped Spiro devices. A recent study has shown that, under low-intensity indoor illumination, the effects of charge trapping and de-trapping at the interface have a prominent role in enhanced J - V hysteresis [30]. Given that the electron transport layer (ETL)/perovskite interface and the perovskite photoactive layer are identical for both the Doped and Undoped Spiro samples, the origin of these interface traps can be attributed to

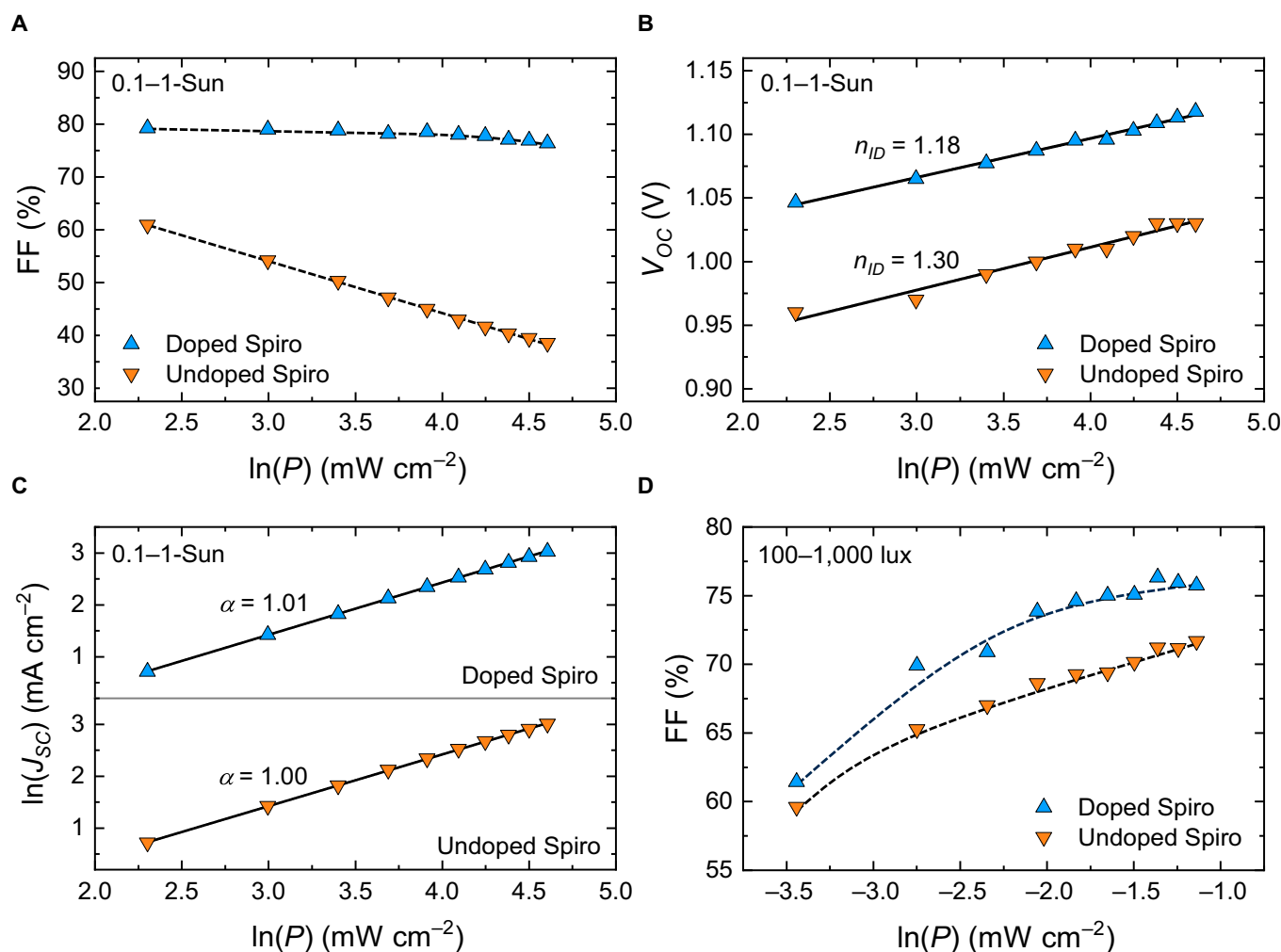


Fig. 3. Light-intensity-dependent photovoltaic parameter variation of Doped Spiro and Undoped Spiro devices. (A) FF variations, (B) semi-log plots of V_{OC} , and (C) log-log plots of J_{SC} versus light intensity (0.1- to 1-Sun). (D) FF variations with light intensity (100 to 1,000 lux).

the differences in the perovskite/HTL buried interface. In the case of Doped Spiro device, the *t*BP dopant is known to deteriorate the perovskite layer at the perovskite|Spiro-OMeTAD interface by forming complexes with PbI₂ [8,31], which leads to the formation of defects or vacancies at the perovskite surface. In addition, the bias-driven diffusion of unoxidized Li⁺ ions from the Li-TFSI dopant through the perovskite layer creates additional shunt pathways and deteriorates the device interfaces [9]. We speculate that most of these defects/traps remain filled at high-light intensities (1-Sun and 1,000 lux) due to the generation of a high number of charge carriers. On the other hand, at very low-light intensities (where the photogenerated charge carriers are in a much lower concentration), there is a considerable number of unfilled traps at the perovskite/HTL interfaces. This contributes to the observed high *J*-*V* hysteresis in this case [32].

To support this claim, open-circuit voltage decay experiments for the Doped Spiro and Undoped Spiro devices were carried out under 2 different light intensities (≈ 0.2 -Sun and ≈ 0.05 -Sun), as shown in Fig. S2A and B. A slower voltage decay is observed for the Undoped Spiro devices under both light intensities but the difference in decay time between the Doped Spiro and Undoped Spiro devices gets reduced at higher light

intensities, indicating that Undoped Spiro devices show a reduction in traps in comparison to their doped equivalents. Charge extraction studies at similar light intensities (see Fig. S2C and D) also support this inference, with the Undoped Spiro devices exhibiting a faster charge extraction at lower light intensity (0.05-Sun) compared to the Doped Spiro devices. Since the large signal open-circuit voltage decay is considered here, the capacitance effects cannot be completely neglected. Hence, an in-depth study on the nature of the charged defects and theoretical calculations on the possible origin of traps and ion migration dynamics in the low-light intensity regime is necessary to further verify our hypothesis. These aspects will be addressed in a future work.

We extracted the ideality factor (n_{ID}) of the Doped Spiro and Undoped Spiro devices by utilizing the semi-logarithmic relation [26] between V_{OC} and incident light intensity under 2 regimes, namely, high-intensity regime (i.e., 0.1- to 1.0-Sun) and low-intensity regime (i.e., 100 to 1,000 lux WLED). In the high-light intensity regime (Fig. 3B), the n_{ID} of 1.18 of the Doped Spiro device is lower than that of the Undoped Spiro counterpart ($n_{ID} = 1.30$). This indicates suppressed non-radiative recombination in the Doped Spiro and agrees with its superior device performance under 1-Sun illumination, although the

Table 2. The photovoltaic parameters of Doped Spiro and Undoped Spiro devices under varying white light-emitting diode (WLED) (4,000 K) illumination intensities

Device	Light intensity	J–V scan direction	PCE(i) (%)	FF (%)	J_{sc} ($\mu\text{A cm}^{-2}$)	V_{oc} (V)	H-index (%)
Doped Spiro	1,000 lux	Reverse	29.1	75.8	129.4	0.95	8.0
		Forward	26.9	72.1	128.6	0.93	
	900 lux	Reverse	28.9	75.9	116.7	0.94	8.1
		Forward	26.7	72.5	115.4	0.92	
	800 lux	Reverse	28.6	76.3	103.2	0.93	8.9
		Forward	26.3	72.4	102.2	0.91	
	700 lux	Reverse	28.0	75.1	89.8	0.93	10.1
		Forward	25.4	71.3	88.8	0.90	
	600 lux	Reverse	27.2	75.0	75.8	0.92	10.7
		Forward	24.6	71.1	74.7	0.89	
	500 lux	Reverse	27.0	74.6	63.6	0.91	11.2
		Forward	24.3	70.3	62.8	0.88	
	400 lux	Reverse	25.9	73.9	49.8	0.90	12.9
		Forward	22.9	68.7	49.6	0.86	
	300 lux	Reverse	24.1	70.9	37.0	0.88	14.9
		Forward	21.0	66.6	36.0	0.84	
	200 lux	Reverse	22.2	69.9	23.6	0.86	19.0
		Forward	18.7	64.1	23.0	0.81	
	100 lux	Reverse	15.8	61.4	10.0	0.82	32.9
		Forward	11.9	50.6	10.0	0.75	
50 lux	Reverse	6.2	41.8	3.4	0.70	41.8	
	Forward	4.4	35.0	3.4	0.59		
Undoped Spiro	1,000 lux	Reverse	25.7	71.7	130.5	0.88	7.7
		Forward	23.9	70.6	130.5	0.83	
	900 lux	Reverse	25.0	71.2	116.4	0.87	6.7
		Forward	23.5	69.9	116.4	0.83	
	800 lux	Reverse	24.7	71.2	102.2	0.87	6.9
		Forward	23.1	70.7	102.2	0.82	
	700 lux	Reverse	24.8	70.2	91.1	0.87	7.0
		Forward	23.2	69.7	90.9	0.82	
	600 lux	Reverse	23.7	69.4	77.1	0.85	6.0
		Forward	22.3	68.5	77.3	0.81	
	500 lux	Reverse	23.2	69.3	63.9	0.84	5.3
		Forward	22.1	68.8	64.1	0.80	
	400 lux	Reverse	22.7	68.6	51.1	0.83	5.2
		Forward	21.6	68.8	50.9	0.79	
	300 lux	Reverse	21.0	67.0	36.6	0.82	5.5
		Forward	19.9	66.8	36.6	0.78	
	200 lux	Reverse	19.8	65.3	24.3	0.80	6.1
		Forward	18.7	66.8	23.8	0.75	
	100 lux	Reverse	15.7	59.6	11.1	0.76	8.4
		Forward	14.5	59.7	11.1	0.70	
50 lux	Reverse	8.6	48.5	4.3	0.67	28.5	
	Forward	6.7	43.0	4.0	0.62		

bimolecular recombination losses in the 2 devices are comparable under short-circuit conditions as shown in the linear J_{SC} -light intensity trends in Fig. 3C. By contrast, an opposite trend of $n_{ID}^{Doped\ Spiro}$ of $2.12 > n_{ID}^{Undoped\ Spiro}$ of 1.98 is observed under WLED illumination (Fig. S3). This suggests a high trap-assisted Shockley-Read-Hall-type recombination dominated by the bulk defects (mid-gap states) in the absorber in both the cases in the low-light intensity regime. Yet, the recombination is more pronounced in the Doped Spiro device, which aligns with our previous discussion suggesting the possibility of a relatively high number of the shunt pathways in this device ($R_{SH} = 0.67 \pm 0.10 \times 10^6 \Omega \text{ cm}^2$ vs. $R_{SH} = 1.21 \pm 0.30 \times 10^6 \Omega \text{ cm}^2$ for the Undoped Spiro device, as calculated from the inverse of the slope of the dark J - V curves at around 0 V).

The Undoped Spiro device delivered a PCE(i) of $\approx 19\%$ at 200 lux, with the corresponding output power of $\approx 12.0 \mu\text{W cm}^{-2}$. So far, the IPV performance of halide perovskites have been mainly reported at 200, 500, and 1,000 lux [11,12,33], with no attention given to performance at lower illuminance levels. Nevertheless, according to several recent studies and the latest characterization standard for IPV's [34–38], it is paramount to report the performance at very low illuminance levels, e.g., 50 lux, since 50 to 400 lux are the most realistic indoor light intensities compatible with the positioning of IoT sensors, with the illuminance levels of ≈ 50 lux measured at the corners of the walls in the indoor environments. At 100 lux, the Undoped Spiro device yielded PCE(i) of $\approx 14\%$ to 15% and V_{OC} of 0.76 V. The output power obtained in this case, in the range of 4.5 to $5.0 \mu\text{W cm}^{-2}$, is comparable to that of many state-of-the-art devices in both emerging and existing IPV technologies [39]. The device also generated a high V_{OC} of 0.67 V even at 50 lux. The notable IPV performance of the Undoped Spiro samples under very low-light intensities down to 50 lux can be attributed to its high R_{SH} of $1.21 \pm 0.30 \times 10^6 \Omega \text{ cm}^2$. The Undoped Spiro devices demonstrated superior performance at very low illumination intensities (i.e., 50 and 100 lux), achieving PCE(i) averages of 7.65% and 15.10% over forward and reverse J - V scans (as shown in Table 2). This is attributed to their reduced trap-assisted recombination and recombination losses (refer to Fig. S2A and B and Fig. S3), as well as more efficient charge extraction (refer to Fig. S2C and D) under reduced light intensity. In comparison, the Doped Spiro devices achieved PCE(i) averages of 5.30% and 13.85% (Table 2). Hence, a pristine (undoped) Spiro-OMeTAD hole-transport material is the best solution for improved and reliable performance at very low-light indoor illuminations. Still, at 50 and 100 lux, the PCE(i) values dropped by 40% and 65%, respectively, with respect to the PCE(i) at 1,000 lux. This is in line with the sudden decrease in the FF below 200 lux. Shunt resistance in the order of $10^7 \Omega \text{ cm}^2$ or higher and low non-radiative recombination in bulk and at the interfaces are entailed to suppress the device shunting and boost FF and V_{OC} , and thus the device performance, even at very low illuminances of ≤ 50 lux [39]. This could be achieved, for example, by reducing the number of pinholes, improving the quality of the absorber layer, and/or employing interfacial passivation strategies. These strategies may also minimize the high H-index of 28.5% of the Undoped device at 50 lux and demonstrate low-hysteresis IPV devices.

It is well-known that the conventional dopants of Spiro-OMeTAD are hygroscopic and release ions that migrate throughout the device layer under bias, thus accelerating the degradation of the corresponding perovskite solar cells [6]. In

this work, we aim at monitoring the stability of our devices employing doped or undoped Spiro-OMeTAD hole-transport material to see if a similar dopant-induced degradation dominates also at low-light intensities. The shelf-life stability in dry air (RH $\approx 15\%$ to 20%) at ≈ 20 to 25°C is monitored up to $\approx 1,700$ h, as shown in Fig. 4A. The Doped Spiro device retains 94% of the initial PCE(i) after the first 400 h owing to the loss in its J_{SC} (Fig. S4). This may be ascribed to the partial degradation of the perovskite layer. However, no further loss in the Doped Spiro device performance is noticed even after 1,700 h of storage. On the other hand, the PCE(i) of Undoped Spiro device initially increases by 4% after 700 h and then by 10% after 1,000 to 1,700 h of storage in the same dry air conditions (Fig. 4A). The enhancement in V_{OC} and FF (notably at the later stage) contributes toward the PCE(i) gain (Fig. S4), which can be attributed to self-doping of Spiro-OMeTAD improving its hole conductivity and energy level alignment with perovskite layer [6,40]. To gain insights into the operational stability of the devices, we monitored their performance at the MPP under continuous WLED illumination for 40 h in N_2 atmosphere. The MPP trends normalized to 1 at the settling time of the tracking algorithm are shown in Fig. 4B. We set the light illuminance value to $\approx 5,000$ lux to guarantee signals with reasonable signal-to-noise ratio. The PCE(i) of the Doped Spiro device remains unchanged during the 40 h, which is different from its behavior under high-intensity 1-Sun illumination (Fig. S5). Instead, the PCE(i) of the Undoped Spiro steadily increases during the initial few hours until it reaches a peak value of 125% after 6 h of the tracking. The efficiency gain of up to 35% to 40% of the initial value is also observed under 1-Sun illumination, as shown in Fig. S5A (the shape of the MPP profile in the 0- to 40-h range is nearly the same for various Undoped Spiro devices tested and follows that of the current density profile). The absolute PCE (1-Sun) of the Undoped Spiro device increases to $\approx 10\%$ from $\approx 6.5\%$ in less than an hour (Fig. S5B). Although the stabilized PCE(i) of 23.4% of the Undoped Spiro at 1,000 lux is lower than the corresponding value for the Doped Spiro device (27.3%), when considering the observed efficiency enhancement factor of 25% (Fig. 4B), its final stabilized PCE(i) will approach a value of $\approx 29.3\%$. Therefore, despite the low initial performance, the resulting IPV efficiency of Undoped Spiro becomes comparable or even higher than that of the Doped Spiro device at 1,000 lux. Similar improvements may be observed even for illumination intensities below 1,000 lux. The inset of Fig. 4B displays the variation of the bias voltage corresponding to the MPP tracking under indoor illumination. The change in the voltage of the Undoped Spiro sample with the tracking time follows that of the PCE(i) and is the highest after 6 h, which indicates that the voltage enhancement contributes to the PCE(i) gain. Light-induced oxidation of Spiro-OMeTAD may not completely explain the high efficiency gain under constant illumination [41]. Alternatively, light-soaking effects (LSE) also influence the photovoltaic device performance under illumination over time. Perovskite solar cells under light soaking typically demonstrate efficiency loss during the day and recovery during the night [42,43]. The opposite effect (type-II LSE) similar to the case of Undoped Spiro devices has also been observed in other photovoltaic systems [42]. Very recently, Du et al. [44] investigated the evolution of J - V characteristics of perovskite solar cells employing undoped Spiro-OMeTAD (vacuum evaporated) under continuous 1-Sun illumination and bias and in the presence of

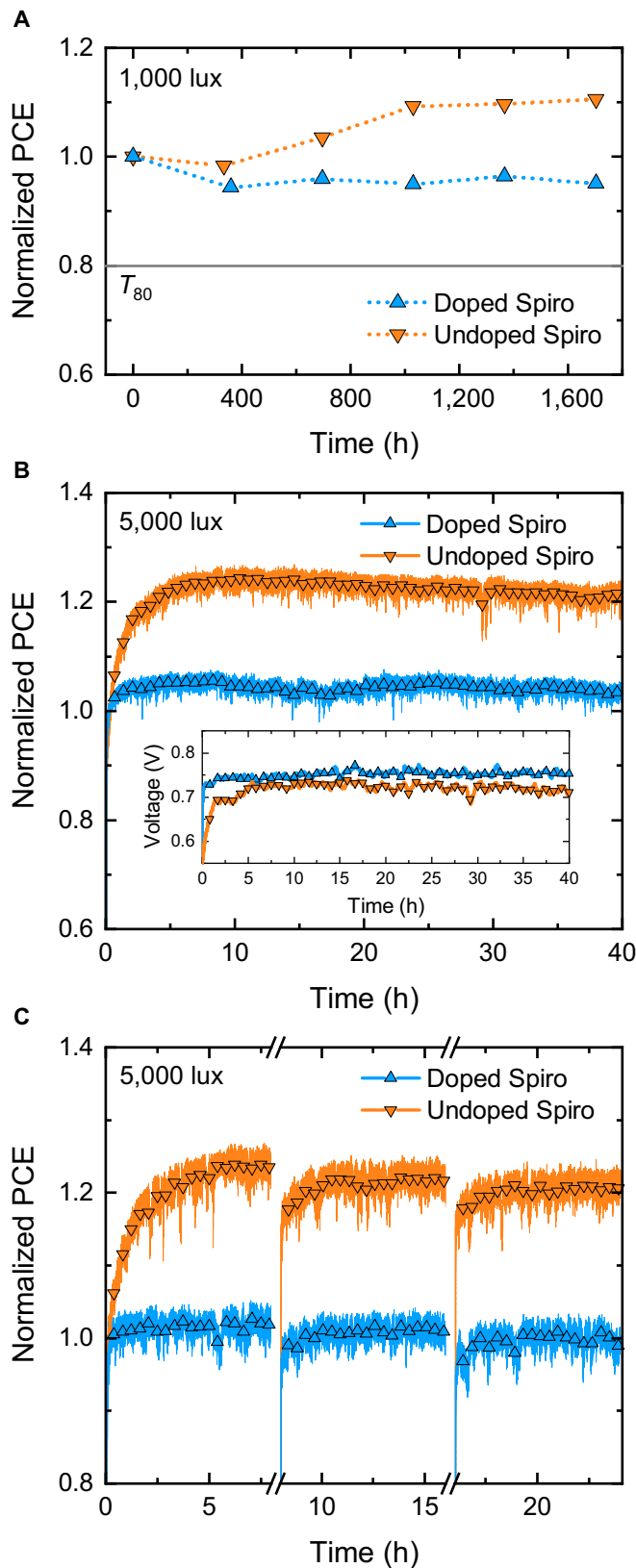


Fig. 4. Stability evaluation of Doped Spiro and Undoped Spiro devices. (A) Shelf-life stability (stored in darkness, RH \approx 15% to 20%) at 1,000 lux; T_{80} represents the time taken by the photovoltaic parameters to approach 80% of their initial values. MPP tracking of Doped Spiro and Undoped Spiro devices under (B) continuous WLED illumination and (C) with light–dark cycles in N_2 environment.

heat. A 30- to 60-min LSE led to a transition of J - V curves from S-shape to square shape. The efficiency of the devices was enhanced by 10 times, mainly due to the substantial improvement in FF and V_{OC} values, and hence attributed to the increased conductivity and hole mobility of the undoped Spiro-OMeTAD HTL, enhanced built-in potential at perovskite|Spiro-OMeTAD interface, and suppressed non-radiative losses in the device [44]. We assign the efficiency and voltage gain observed from our long-term MPP tracking measurements to the LSE. Also, the accelerated PCE saturation under 1-Sun illumination may be attributed to its high-light intensity compared to the low-light intensity of the indoor lighting. Furthermore, we conducted indoor light cycling measurements (8 h in light and 16 h in dark) similar to those recently proposed under 1-Sun illumination [45,46]. After keeping the device in the dark for 16 h, the efficiency gain under illumination is comparable among the 3 light–dark cycles, but the rate at which the gain took place is higher for the last 2 cycles (Fig. 4C). Although this suggests that the observed LSE-based efficiency enhancement is reversible in nature with degradation during the night and recovery during the day, special attention is required to understand the influence of the stress factors such as illumination intensity, spectral shape, time, temperature, and electric bias on the efficiency gain under the continuous and light cycle-based MPP tracking. On the other hand, the Doped Spiro sample showed a stable PCE trend with negligible changes under constant illumination of indoor WLED light (Fig. 4B), although it degraded under 1-Sun illumination (Fig. S5). Therefore, no LSE-based PCE improvement took place in this case, which can be attributed to the Li^+ (in Li-TFSI) diffusion-driven or tBP -mediated corrosion and degradation of the perovskite layer under applied bias and constant illumination [8,31,44].

Conclusion

Herein, we examined the variations in performance trends of triple-cation LHP photovoltaic cells, employing a pristine (undoped) or doped Spiro-OMeTAD HTL, when exposed to different light conditions, specifically under simulated solar light (1-Sun) and low-intensity artificial WLED illuminations. Despite the known low performance of the Undoped Spiro cells under 1-Sun illumination, a remarkable PCE(i) up to 25.6% is observed at 1,000 lux WLED lighting, mainly due to the enhanced FF at low-light intensity. The diminished influence of the series resistance (typically high for Undoped Spiro devices) on the FF at the low-light intensity explains the enhanced device performance of the Undoped Spiro under indoor illumination. Although the initial PCE(i) of the Undoped Spiro device at 1,000 lux is slightly lower than that of the Doped Spiro device, upon constant illumination for 6 h and under applied bias (MPP condition), the final PCE(i) value is drastically increased due to the light-soaking effect. Moreover, while the J - V hysteresis behavior of the Doped Spiro intensifies under very low WLED intensities, this phenomenon is not observed in the Undoped Spiro samples. Furthermore, the Undoped Spiro devices suffer low voltage losses with reducing light intensity and deliver V_{OC} values in the 0.67 to 0.76 V range even at 50 to 100 lux. In contrast to the well-established practice of using doped Spiro-OMeTAD HTL for high-efficiency LHP-based solar cells, our findings suggest that dopants in Spiro-OMeTAD HTL may not be necessary for the fabrication of stable and efficient indoor photovoltaics.

Our work underscores that the efficiency of LHP-based solar cells under 1-Sun illumination does not automatically predict their performance under the low-light intensity conditions of artificial indoor lighting. Although a solid understanding of optimized solar cell parameters is essential toward high-performance LHP indoor photovoltaic devices, it is the further refinement of various device layers and interfaces, specifically tailored to low-intensity indoor lighting, that is pivotal to unlocking efficient and stable indoor photovoltaics.

Acknowledgments

Funding: S.T. and P.V. acknowledge the financial support of the Jane and Aatos Erkkö Foundation within the SOL-TECH project. P.V. also thanks Academy of Finland, Decision No. 347772. G.K.G. thanks Tampere Institute for Advanced Study for the postdoctoral funding. B.A.-A. thanks the Vilho, Yrjö, and Kalle Väisälä Fund of the Finnish Academy of Science and Letters for the financial support. This work was part of the Academy of Finland Flagship Programme, Photonics Research, and Innovation (PREIN), Decision No. 320165. This work made use of Tampere Microscopy Center facilities at Tampere University.

Author contributions: S.T.: Investigation, data curation, formal analysis, validation, visualization, methodology, and writing—review and editing. G.K.G.: Conceptualization, investigation, data curation, visualization, methodology, funding acquisition, and writing—original draft. S.W.: Investigation, data curation, formal analysis, visualization, methodology, and writing—review and editing. B.B.: Investigation, data curation, formal analysis, visualization, and methodology. B.A.-A.: Investigation, data curation, formal analysis, visualization, and methodology. L.K.J.: Formal analysis, methodology, resources, supervision, validation, and writing—review and editing. P.V.: Conceptualization, methodology, funding acquisition, project administration, resources, supervision, validation, and writing—original draft.

Competing interests: The authors declare that they have no competing interests.

Data Availability

Data are freely available upon request.

Supplementary Materials

Figs. S1 to S5
Table S1

References

- Best Research-Cell Efficiency Chart | Photovoltaic Research | NREL [accessed 6 Dec 2023] <https://www.nrel.gov/pv/cell-efficiency.html>
- Cahen D, Kronik L, Hodes G. Are defects in lead-halide perovskites healed, tolerated, or both? *ACS Energy Lett.* 2021;6(11):4108–4114.
- Park J, Kim J, Yun H-S, Paik MJ, Noh E, Mun HJ, Kim MG, Shin TJ, Seok SI. Controlled growth of perovskite layers with volatile alkylammonium chlorides. *Nature.* 2023;616(7958):724–730.
- Kim JY, Lee J-W, Jung HS, Shin H, Park N-G. High-efficiency perovskite solar cells. *Chem Rev.* 2020;120(15):7867–7918.
- Leijtens T, Lim J, Teuscher J, Park T, Snaith HJ. Charge density dependent mobility of organic hole-transporters and mesoporous TiO₂ determined by transient mobility spectroscopy: Implications to dye-sensitized and organic solar cells. *Adv Mater.* 2013;25(23):3227–3233.
- Liu M, Dahlström S, Ahläng C, Wilken S, Degterev A, Matuhina A, Hadadian M, Markkanen M, Aitola K, Kamppinen A, et al. Beyond hydrophobicity: How F4-TCNQ doping of the hole transport material improves stability of mesoporous triple-cation perovskite solar cells. *J Mater Chem A Mater.* 2022;10:11721–11731.
- Rombach FM, Haque SA, Macdonald TJ. Lessons learned from Spiro-OMeTAD and PTAA in perovskite solar cells. *Energy Environ Sci.* 2021;14(10):5161–5190.
- Li W, Dong H, Wang L, Li N, Guo X, Li J, Qiu Y. Montmorillonite as bifunctional buffer layer material for hybrid perovskite solar cells with protection from corrosion and retarding recombination. *J Mater Chem A Mater.* 2014;2(33):13587–13592.
- Li Z, Xiao C, Yang Y, Harvey SP, Kim DH, Christians JA, Yang M, Schulz P, Nanayakkara SU, Jiang C-S, et al. Extrinsic ion migration in perovskite solar cells. *Energy Environ Sci.* 2017;10(5):1234–1242.
- Zhu H, Teale S, Lintangpradipto MN, Mahesh S, Chen B, McGehee MD, Sargent EH, Bakr OM. Long-term operating stability in perovskite photovoltaics. *Nat Rev Mater.* 2023;8(9):569–586.
- Wang K-L, Lu H, Li M, Chen C-H, Bo Zhang D, Chen J, Wu J-J, Zhou Y, Wang X, Su Z. Ion-dipole interaction enabling highly efficient CsPbI₃ perovskite indoor photovoltaics. *Adv Mater.* 2023;35(31):Article 2210106.
- Guo Z, Jena AK, Miyasaka T. Halide perovskites for indoor photovoltaics: The next possibility. *ACS Energy Lett.* 2022;8(1):90–95.
- Mathews I, Kantareddy SN, Buonassisi T, Peters IM. Technology and market perspective for indoor photovoltaic cells. *Joule.* 2019;3(6):1415–1426.
- Wang S, Edwards PR, Abdelsamie M, Brown P, Webster D, Ruseckas A, Rajan G, Neves AIS, Martin RW, Sutter-Fella CM, et al. Chlorine retention enables the indoor light harvesting of triple halide wide bandgap perovskites. *J Mater Chem A.* 2023;11:12328–12341.
- Skafi Z, Xu J, Mottaghitalab V, Mivehi L, Taheri B, Jafarzadeh F, Podapangi SK, Altamura D, Guascito MR, Barba L, et al. Highly efficient flexible perovskite solar cells on polyethylene terephthalate films via dual halide and low-dimensional Interface engineering for indoor photovoltaics. *Sol RRL.* 2023;7(20):2300324.
- Kim S, Jahandar M, Jeong JH, Lim DC. Recent progress in solar cell technology for low-light indoor applications. *Curr Altern Energy.* 2019;3(1):3–17.
- Saliba M, Matsui T, Seo J-Y, Domanski K, Correa-Baena J-P, Nazeeruddin MK, Zakeeruddin SM, Tress W, Abate A, Hagfeldt A, et al. Cesium-containing triple cation perovskite solar cells: Improved stability, reproducibility and high efficiency. *Energy Environ Sci.* 2016;9(6):1989–1997.
- Peng Y, Huq TN, Mei J, Portilla L, Jagt RA, Occhipinti LG, Macmanus-driscoll JL, Hoyer RLZ, Pecunia V. Lead-free perovskite-inspired absorbers for indoor photovoltaics. *Adv Energy Mater.* 2020;11(1):2002761.
- Rühle S. Tabulated values of the Shockley–Queisser limit for single junction solar cells. *Sol Energy.* 2016;130:139–147.

20. Noh JH, Jeon NJ, Choi YC, Nazeeruddin MK, Grätzel M, Seok SI. Nanostructured $\text{TiO}_2/\text{CH}_3\text{NH}_3\text{PbI}_3$ heterojunction solar cells employing Spiro-OMeTAD/co-complex as hole-transporting material. *J Mater Chem A*. 2013;1(38):11842–11847.
21. Habisreutinger SN, Noel NK, Snaith HJ, Nicholas RJ. Investigating the role of 4-tert butylpyridine in perovskite solar cells. *Adv Energy Mater*. 2017;7(1):1601079.
22. Scholin R, Karlsson MH, Eriksson SK, Siegbahn H, Johansson EMJ, Rensmo H. Energy level shifts in Spiro-OMeTAD molecular thin films when adding Li-TFSI. *J Phys Chem C*. 2012;116(50):26300–26305.
23. Chen B, Yang M, Priya S, Zhu K. Origin of J–V hysteresis in perovskite solar cells. *J Phys Chem Lett*. 2016;7(5):905–917.
24. Tress W, Marinova N, Moehl T, Zakeeruddin SM, Nazeeruddin MK, Grätzel M. Understanding the rate-dependent J–V hysteresis, slow time component, and aging in $\text{CH}_3\text{NH}_3\text{PbI}_3$ perovskite solar cells: The role of a compensated electric field. *Energy Environ Sci*. 2015;8(3):995–1004.
25. Xu J, Reddy SH, Castriotta LA, Podapangi SK, Luce M, Cricenti A, Di Carlo A, Brown TM. 30% efficient triple-cation perovskite solar cells under indoor illumination enabled by rare earth EuCl_3 doping. *Sustain Energy Fuel*. 2023;7:3404–3411.
26. Glowienka D, Galagan Y. Light intensity analysis of photovoltaic parameters for perovskite solar cells. *Adv Mater*. 2022;34(2):e2105920.
27. Ho JKW, Yin H, So SK. From 33% to 57%—An elevated potential of efficiency limit for indoor photovoltaics. *J Mater Chem A Mater*. 2020;8(4):1717–1723.
28. Zhao Y-C, Zhou W-K, Zhou X, Liu K-H, Yu D-P, Zhao Q. Quantification of light-enhanced ionic transport in Lead iodide perovskite thin films and its solar cell applications. *Light Sci Appl*. 2017;6(5):Article e16243.
29. Pazoki M, Jacobsson TJ, Cruz SHT, Johansson MB, Imani R, Kullgren J, Hagfeldt A, Johansson EMJ, Edvinsson T, Boschloo G. Photon energy-dependent hysteresis effects in lead halide perovskite materials. *J Phys Chem C*. 2017;121(47):26180–26187.
30. Bulloch A, Wang S, Ghosh P, Jagadamma LK. Hysteresis in hybrid perovskite indoor photovoltaics. *Phil Trans R Soc A*. 2022;380(2221):Article 20210144.
31. Han Y, Zhang G, Xie H, Kong T, Li Y, Zhang Y, Song J, Bi D. Azide additive acting as a powerful locker for Li^+ and TBP in Spiro-OMeTAD toward highly efficient and stable perovskite solar cells. *Nano Energy*. 2022;96:Article 107072.
32. Han EQ, Lyu M, Choi E, Zhao Y, Zhang Y, Lee J, Lee S, Jiao Y, Ahmad SHA, Seidel J, et al. High-performance indoor perovskite solar cells by self-suppression of intrinsic defects via a facile solvent-engineering strategy. *Small*. 2023;20(4):Article 2305192.
33. Dagar J, Castro-Hermosa S, Lucarelli G, Cacialli F, Brown TM. Highly efficient perovskite solar cells for light harvesting under indoor illumination via solution processed SnO_2/MgO composite electron transport layers. *Nano Energy*. 2018;49:290–299.
34. Reynaud CA, Clerc R, Lechene PB, Hebert M, Cazier A, Arias AC. Evaluation of indoor photovoltaic power production under directional and diffuse lighting conditions. *Sol Energy Mater Sol Cells*. 2019;200:Article 110010.
35. Kauer M, Bellanger M. Bellanger M. High-efficiency indoor photovoltaic energy harvesting. In: *Indoor photovoltaics*. USA: John Wiley & Sons, Incorporated; 2020. p. 213–239.
36. Huntley R. Ambient light harvesting heads indoors. *EE Times Europe*. 17 Nov 2023. <https://www.eetimes.eu/ambient-light-harvesting-heads-indoors/>
37. Grandhi GK, Toikkonen S, Al-Anesi B, Pecunia V, Vivo P. Perovskite-inspired $\text{Cu}_2\text{AgBiI}_6$ for mesoscopic indoor photovoltaics under realistic low-light intensity conditions. *Sustain Energy Fuels*. 2023;7(1):66–73.
38. IEC. Nanomanufacturing - Key control characteristics - Part 7-2: Nano-enabled photovoltaics - Device evaluation method for indoor light. IEC TS 62607-7-2:2023. <https://webstore.iec.ch/publication/61819>
39. Müller D, Jiang E, Rivas-Lazaro P, Baretzky C, Loukeris G, Bogati S, Paetel S, Irvine SJC, Oklobia O, Jones S, et al. Indoor photovoltaics for the internet-of-things—A comparison of state-of-the-art devices from different photovoltaic technologies. *ACS Appl Energy Mater*. 2023;6(20):10404–10414.
40. Zhang Y, Wu F, Chen L, Zhang F, Ji Y, Shen W, Li M, Guo Q, Su W, He R. Molecular engineering of highly efficient dopant-free Spiro-type hole transporting materials for perovskite solar cells. *Sol Energy Mater Sol Cells*. 2020;212:Article 110534.
41. Sanchez RS, Mas-Marza E. Light-induced effects on Spiro-OMeTAD films and hybrid lead halide perovskite solar cells. *Sol Energy Mater Sol Cells*. 2016;158:189–194.
42. Wang J, Duan X, Yin W-J. Photoinduced dynamic defects responsible for the giant, reversible, and bidirectional light-soaking effect in perovskite solar cells. *J Phys Chem Lett*. 2021;12(38):9328–9335.
43. Hartono NTP, Köbler H, Graniero P, Khenkin M, Schlatmann R, Ulbrich C, Abate A. Stability follows efficiency based on the analysis of a large perovskite solar cells ageing dataset. *Nat Commun*. 2023;14(1):4869.
44. Du G, Yang L, Zhang J. Light soaking induced halide doping of evaporated Spiro-OMeTAD in perovskite solar cells. *Laser Photon Rev*. 2023;17(1):2200475.
45. Abate A. Stable tin-based perovskite solar cells. *ACS Energy Lett*. 2023;8(4):1896–1899.
46. Khenkin MV, Köbler H, Remec M, Roy R, Erdil U, Li J, Phung N, Adwan G, Paramasivam G, Emery Q. Light cycling as a key to understanding the outdoor behaviour of perovskite solar cells. *Energy Environ Sci*. 2023;17:602–610.